Theses and Dissertations

August 2015

Tin Nanoparticles Encapsulated in Hollow TIO2 Spheres as High Performance Anode Materials for Li-Ion Batteries

Xiang Pan
University of Wisconsin-Milwaukee

Recommended Citation

TIN NANOPARTICLES ENCAPSULATED IN HOLLOW TIO$_2$ SPHERES AS HIGH PERFORMANCE ANODE MATERIALS FOR LI-ION BATTERIES

by

Xiang Pan

A Thesis Submitted in

Partial Fulfillment of the

Requirements for the Degree of

Master of Science

in Engineering

at

The University of Wisconsin-Milwaukee

August 2015

ABSTRACT

TIN NANOPARTICLES ENCAPSULATED IN HOLLOW TIO$_2$ SPHERES AS HIGH PERFORMANCE ANODE MATERIALS FOR LI-ION BATTERIES

by

Xiang Pan

The University of Wisconsin-Milwaukee, 2015
Under the Supervision of Professor Junhong Chen

Tin, an anode material with a high capacity for lithium-ion batteries, has poor cyclic performance because of the high volume expansion upon lithiation. Based on a literature review of the applications of lithium-ion batteries and current research progress of the tin-based anode materials for lithium-ion batteries, we developed a method to synthesize hollow TiO$_2$ spheres with tin nanoparticles anchored on the inner surface of the TiO$_2$ shell. Such a unique tin/TiO$_2$ composite alleviates the volume change of tin–based anode materials in charge-discharge processes. SnCl$_2$·2H$_2$O (Tin (II) chloride dihydrate) and titanium (IV) isopropoxide (TIPT) were used as the Sn source and the Ti source, respectively, while CaCO$_3$ was used as a template to fabricate the TiO$_2$ hollow shell. A variety of modern material testing methods (XRD, SEM, XPS, Raman, BET, etc.) and

electrochemical measurements such as galvanostatic charge-discharge and cyclic voltammetry (CV) testing were employed to systematically study effects of various synthesis parameters on the structure and battery performance of the as-prepared materials. We also discussed the key factors influencing the cycle performance of the composite electrode material and the related mechanism.

iv

TABLE OF CONTENTS

LIST OF FIGURES

LIST OF TABLES

LIST OF ABBREVIATIONS

CMC….….…Carboxy Methylated Cellulose

CV……………Cyclic Voltammetry

DI Water……...De-ionized water

EDS…………...Energy-dispersive X-ray Spectroscopy

EIS……………Electrochemical Impedance Spectroscopy

FEC…………....Fluoroethylene Carbonate

LIB…………....Lithium-ion Battery

LTO…………... Lithium Titanium Oxide

MCMB……..….Mesophase Carbon Micro Beads

NMP………..….N-Methyl-2-Pyrrolidone

NWs…………...Nanowires

PAA………….. Poly (Acrylic Acid)

PE……………..Polyethylene

PP……………..Polypropylene

SBR………….. Styrene-Butadiene Rubber

SEM…………..Scanning Electron Microscopy

TIPT…………..Titanium (IV) Isopropoxide

VC……………Vinylene Carbonate

XRD…………..X-ray Diffraction

XPS………….. X-ray Photoelectron Spectrometer

ACKNOWLEDGEMENTS

I would like to thank my advisor, Professor Junhong Chen, for his support thoughout my graduation project. His encouragement is the power to let me go the distance. The weekly group meeting also inspired me to make greater progress.

I also want to express my gratitude to Dr. Xingkang Huang, who is the man who gave me a guiding hand on experiments and paper work. My work would not have been possible without his meticulous guidance. His rigorous academic attitude educated me on what is a researcher should be like.

My appreciation goes out to Professor Benjamin Church, Professor Nidal Abu-Zahra and other professors in the College of Engineering & Applied Science. You always give me pertinent advice when I was facing a tough choice.

I have to show my appreciation to senior students in Professor Chen's group, like Guihua Zhou, Xiaoru Guo, et al. They helped me a lot in the lab and regarded me as a friend in the daily life. I would like to thank Miss Gwen Barker, who was working for Johnson Controls, for training me on many instruments used for lithium-ion battery fabrication and characterization. My deep gratitude goes out to Dr. Steven Hardcastle for training me on analytical instruments in the Advanced Analysis Facility, as well Professor Deyang Qu for allowing me to use the experimental apparatus in his lab, EMS 810.

Finally, I would love to dedicate the last sentence to my parents and my partner who give me unconditional support. I am willing to do everything I can to make you proud.

1. Background

It is imperative to solve the problem of energy shortages and the increasingly serious environmental pollution problems. Various high energy batteries will play a more important role in the future. The existing rechargeable batteries mainly include lead-acid batteries, nickel cadmium batteries, nickel metal hydride batteries, and lithium-ion (Li-ion) batteries (LIBs). The Li-ion batteries attract tremendous attention because of the advantages of high energy density, high average output voltage, low self-discharge, broad operating temperature range, no memory effect, a long cycle life, and less pollution compared with lead-acid batteries. Since the birth of the LIB prototype, researchers have never stopped improving the performance of LIBs. Along with the advancement of technology, the performance of LIBs has been significantly enhanced. Now LIBs have been widely used in mobile phones, notebook computers, and portable electronic devices.

1.1 Lithium-ion Battery (LIB)

Lithium-ion batteries that have high energy density in all kinds of green secondary batteries, have been widely used in notebook computers, mobile phones, and other consumer electronics products. With the rapid development of wireless communications products, electric cars, and electric tools, an urgent need has been developed to improve the energy density, power density and life performance of lithium-ion battery electrode materials.

1.2 Principle of lithium-ion batteries
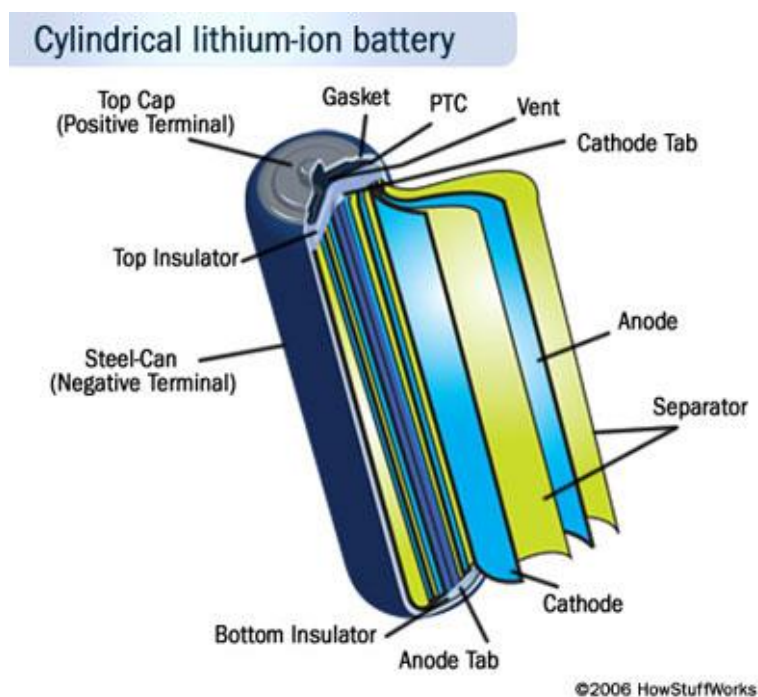
Figure 1 Internal structure of cylindrical lithium-ion battery (Reprinted courtesy of HowStuffWorks.com)

The LIB is one of the rechargeable secondary batteries in which Li^+ can be inserted into and extracted from cathode and anode materials. The internal structure of a cylindrical LIB is shown in Figure 1. Actually it is a concentration cell, with embedded lithium compounds always used as a cathode, such as $LiCoO_2$ and $LiMn_2O_4$. Graphite is commonly used as an anode electrode, and organic solvents with lithium salt ($LiFP_6$, $LiAsF_6$) are common for the electrolyte. Both electrodes allow lithium ions to move in and out of their interiors. During insertion (or intercalation) lithium ions move into the electrode. During the reverse process, lithium ions move back out. When a lithium-ion based cell is discharging, the positive lithium ion moves from the negative electrode and enters the positive electrode. The sketches of the charge/discharge processes are shown in Figure 2.
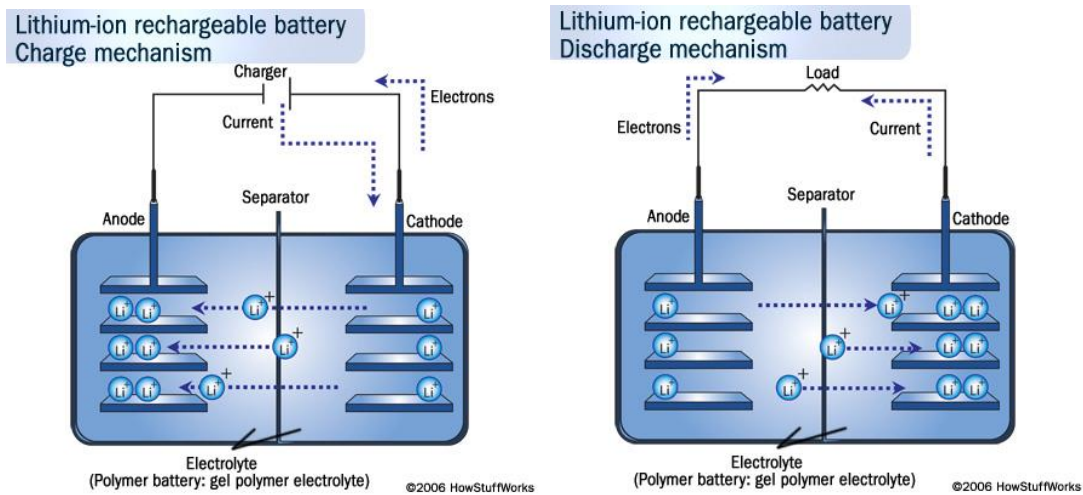
Figure 2 Lithium-ion batteries charge and discharge mechanism sketches (Reprinted courtesy of HowStuffWorks.com)

The following equations show one example of the chemistry:

The positive electrode half-reaction is:

$$LiCoO_2 \leftrightarrow Li_{1-x}CoO_2 + xLi^+ + xe^- \qquad (1)$$
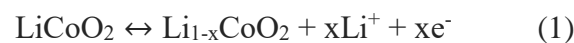
The negative electrode half reaction is:

$$xLi^+ + xe^- + xC_6 \leftrightarrow xLiC_6 \qquad (2)$$

The overall reaction has its limits. Over discharge supersaturates lithium cobalt oxide, leading to the production of lithium oxide [2] possibly by the following irreversible reaction:

$$Li^+ + e^- + LiCoO_2 \leftrightarrow Li_2O + CoO \qquad (3)$$
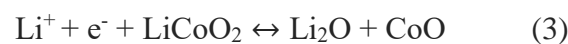
1.3 Tin (Sn) based materials for LIBs

Sn and Li can form $Li_{4.4}$ Sn alloy, whose high theoretical specific capacity (993.4 mAh g^{-1}) [36] has attracted widespread attention. However, a Li-Sn alloy is accompanied by huge volume expansion, so the cycle performance is unsatisfying, limiting its practical application.

2 Literature Review

At present, lithium-ion battery anode materials generally use carbon materials, such as graphite, hard carbon, etc. Other than carbon anode materials, nitrides, lithium-ion oxides, transition metal oxide, silicon materials, tin base material and some other new alloy materials are also used. Some main parameters of various anode materials are given in Table 1. Potential vs. Li/Li^+ and the corresponding capacity density of some potential anode active materials are displayed in Figure 3. Nanoscale materials, because of their unique performance, also have received widespread attention in the studies of anode materials.

Table 1 Comparison of the theoretical specific capacity, charge density, volume change and onset potential of various anode materials.

Materials	Li	C	$Li_4Ti_5O_{12}$	Si	Sn	Sb	Al	Mg	Bi
Density ($g\ cm^{-3}$)	0.53	2.25	3.5	2.33	7.29	6.7	2.7	1.3	9.78
Lithiated phase	Li	LiC_6	$Li_7Ti_5O_{12}$	$Li_{4.4}Si$	$Li_{4.4}Sn$	Li_3Sb	LiAl	Li_3Mg	Li_3Bi
Theoretical specific capacity ($mAh\ g^{-1}$)	3862	372	175	4200	994	660	993	3350	385
Theoretical charge density ($mAh\ cm^{-3}$)	2047	837	613	9786	7246	4422	2681	4355	3765
Volume change (%)	100	12	1	320	260	200	96	100	215
Potential vs. Li (~V)	0	0.05	1.6	0.4	0.6	0.9	0.3	0.1	0.8
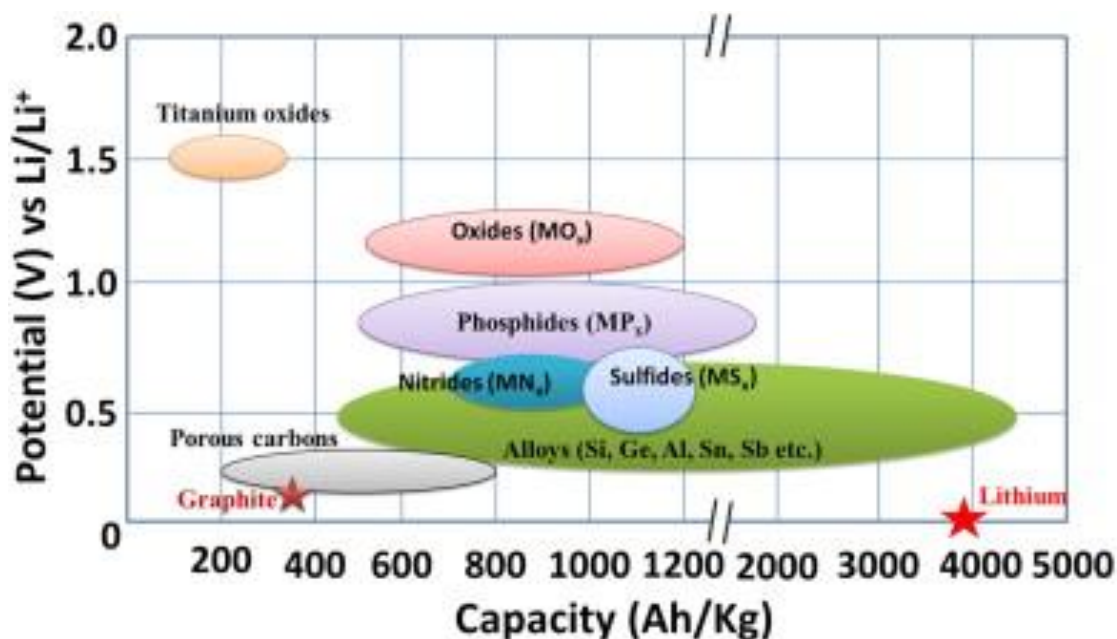
Figure 3 Schematic illustration of active anode materials for the next generation of lithium batteries. Potential *vs.* Li/Li$^+$ and the corresponding capacity density are shown [7].

2.1 Carbon anode materials

A carbon anode of lithium-ion batteries in terms of safety and cycle life shows better performance, and carbon materials are cheap and non-toxic; so they are widely used in commercial lithium-ion battery anode materials. Commercially developed lithium-ion battery anode materials mainly include graphite, petroleum coke, carbon fiber, pyrolysis, Mesophase Carbon Micro Beads (MCMB), carbon black, carbon glass, etc. Carbon anode materials are divided into graphite and amorphous carbon materials; they are all made of graphite crystallite, but their crystallinity is different; some other structural parameters are different also. So, their chemical and physical properties and electrochemical properties show different features.

Graphite is definitely the most used anode [3-6] owing to its excellent features, such as flat and low working potential vs. lithium, low cost and good cycle life. However, graphite allows the intercalation of only one Li-ion with six carbon atoms, with a

resulting stoichiometry of LiC_6 and thus an equivalent reversible capacity of 372 mAh g^{-1} [7]. It also is sensitive to the composition of the electrolyte, and organic solvent compatible ability is poor; only a small number of electrolyte has good electrochemical performance, and the resistance to overcharge ability is poor. During the process of charging and discharging, solvent molecules may be embedded into the graphite, which easily ruins the graphite structure. In addition, the diffusion coefficient of lithium ions in the graphite is small.

Amorphous carbon has high capacity and the discharge performance under large current is good, with a de-intercalation capacity up to more than 900 mAh g^{-1}. But high first irreversible capacity and voltage hysteresis limits the performance of amorphous carbon materials. In addition, the cycle performance is not ideal, with reversible capacity dropping rapidly upon cycling. Both the graphite and amorphous carbon material have their advantages and disadvantages; they have been investigated extensively to improve their electrochemical performance.

2.2 Silicon (Si) based anode materials

Silicon has both the highest gravimetric capacity (4,200 mAh g^{-1}, $Li_{22}Si_5$) and volumetric capacity (9,786 mAh cm^{-3}) among the anode material candidates [8-12].

In addition, the discharge (lithiation) potential of silicon is a little higher than that of graphite, 0.4 V vs. Li^+/Li. Therefore, it has less chance to develop dendrite on the Si anode, compared with the graphite anodes during the process of charging and discharging, which means a better safety performance. The electrochemical lithiation

of Si electrodes has been deeply investigated by many groups. It has been clarified that the high specific capacity value is due to the formation of intermetallic Li–Si binary compounds such as $Li_{12}Si_7$, Li_7Si_3, $Li_{13}Si_4$, $Li_{22}Si_5$[7]. However, the main drawback of silicon-based anode materials is the poor cycle stability, because of the large volume change (~400%) in alloying and dealloying, resulting in pulverization and spalling of electrode materials.

To overcome these problems, nanowires, nanotubes and nanospheres were considered due to their capability of providing the necessary free volume for accommodating the Si expansion during the alloying/de-alloying process. In particular, Si nanowires (Si NWs) and nanotubes have shown a reversible capacity over 2,000 mAh g^{-1} with good cycling stability. [7]

SiO is considered an alternative choice to silicon as an anode candidate, although its theoretical capacity (>1,600 mAh g^{-1}) is lower than that of Si. In addition, lithium oxygen co-ordination implies minimal volume change and, at the same time, lower activation energy [13-16]. The mechanism can be expressed as follows:

$$xLi + SiO \leftrightarrow Li_x–ySi_z + Li_xSiO_z \qquad (4)$$
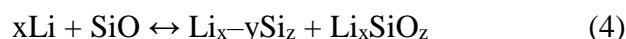
The effects of both the oxygen concentration and the particle size on the cycling life and on the reversible capacity of SiO_x were studied [17]. Different oxygen concentrations of SiO, such as $SiO_{0.8}$, SiO and $SiO_{1.1}$, along with the particle size, such as 30 and 50 nm, were prepared. It was observed that $SiO_{0.8}$ with 50 nm particle size shows a high capacity of 1,700 mAh g^{-1} at initial cycles, but along with large capacity falling over cycling [17]. However, $SiO_{1.1}$ can maintain a stable capacity over cycling of 750 mAh g^{-1}. The conclusion was that lower oxygen contents in SiO_x indicate higher specific

capacity but also cause poorer cycling life. In addition, 30 nm SiO_x particle size showed better capacity retention with high reversible capacity compared with larger particles.

2.3 Nitrides

Nitrides as lithium-ion battery anode materials have been researched mainly because of the high conductivity of Li_3N. The product by the reaction of Li_3N and transition metal is lithium transition metal nitrides. It basically has two kinds of structure: anti-fluorite structure and Li_3N structure, both have very good ionic conductivity, electronic conductivity and chemical stability. The electrochemical performance and the lithium insertion/removal capacity of titanium-based oxides mainly depend on the different kinds of materials. Gillot et al. prepared Ni_3N by various synthetic routes, such as ammonolysis of nickel salts, or nickel particles, and thermal decomposition of nickel-amide in the presence of ammonia [29]. Ni_3N from nickel-amide showed the best electrochemical performances, with the largest capacity (1,200 mAh g^{-1}) [7].

2.4 Spinel $Li_4Ti_5O_{12}$ (LTO)

LTO has generated significant interest for researchers because of the excellent Li-ion reversibility at the high operating potential of 1.55 V (vs .Li/Li$^+$). The high operating potential guarantees safety conditions; in fact, the formation of the solid electrolyte interphase (SEI) is mitigated and the development of dendrites, a typical issue in carbon-based anodes, is avoided [30]. But the low specific capacity limits the application of LTO materials. Researchers have considered that enhancing the electronic

conductivity of LTO by surface treatments [31-32], and enhancing the Li-ion diffusion by downsizing the LTO to the nanoscale [7].

2.5 Tin based anode materials

Tin has reversible alloying and dealloying reaction with lithium, forming and decomposing the alloy phase Li_xSn_y, including LiSn, Li_2Sn_5, Li_7Sn_3, Li_5Sn_2, Li_7Sn_2, $Li_{13}Sn_5$ and $Li_{22}Sn_5$. LiSn and Li_2Sn_5 are layered crystal structures, while others can hardly form a long-range order crystal structure [18].

As a lithium metal alloy anode material, Sn has received widespread attention once proposed. Its main advantage is high specific capacity (993 mAh g^{-1}), which is twice that of the graphite. However, like other metal alloy anode materials, a huge volume change accompanies the alloying and de-alloying process, which leads to stress and pulverization of active materials, finally resulting in a poor cycle performance.

Tin oxide was first developed by Fuji Photo film corporation[7] and it received significant attention as an anode for Li-ion batteries due to the high theoretical capacity and low work potential, i.e., 0.6 V vs. Li/Li^{+}[19-22]. The electrochemical lithium alloying reactions can be summarized in a first partially irreversible step, where SnO_2 is reduced into Sn and lithium oxides ($SnO_2+4Li \leftrightarrow Sn+2Li_2O$), which is followed by the reversible Sn–lithium alloying/de-alloying reaction ($Sn+4.4Li^+ \leftrightarrow Li_{4.4}Sn$). This overall electrochemical process involves 8.4 Li for one SnO_2 formula unit [7]. The corresponding theoretical capacity is 1,491 mAh g^{-1} but it is reduced to 783 mAh g^{-1} when the second highly reversible step is reached. Hence, 783 mAh g^{-1} is commonly

considered as the actual theoretical capacity. However, it has the same problem as other Sn-based materials; volume change will crash the structure, resulting in a quick capacity decay upon cycling.

Therefore, the main issue to be addressed is how to reduce the effect of volume expansion and improve the cycle performance. Porous nanostructures, nanocomposites, and hollow nanostructured Sn/SnO_2 have been proposed to overcome the above specified issues [23-25]. Porosity in nanostructured SnO_2 is capable of balancing the volume changes during the lithium insertion/de-insertion. These pores act as a buffer for the large volume changes. Yin et al. prepared SnO_2 mesoporous spheres in the range of 100–300 nm from tin sulphate, by a cost-effective and easy solution method. These prepared SnO_2 spheres delivered capacities of 761 and retained 480 mAh g^{-1} after 50 charge–discharge cycles at current densities of 200 mA g^{-1} and 2,000 mA g^{-1}, respectively [26].

SnO_2/C were also proposed considering the wide use of carbon in LIBs. Carbon-free and carbon-coated SnO_2 hollow microspheres were prepared through a cost-effective hydrothermal route where glucose was used as a carbon source [25]. The results showed better performance for the carbon-coated SnO_2, in terms of storage capacity, Coulombic efficiency and cycling life [7].

More and more researchers are now paying close attention to some specific Sn - based composite materials. Zhang et al. [27] prepared hollow carbon spheres to supply the shell for Sn nanoparticles, with a synthetic scheme presented in Figure 4. This work improved the cycle performance (800 mAh g^{-1} in the initial 10 cycles, and 550 mAh g^{-}

[1] after 100 cycles). Liao et al. [28] prepared three- dimensional mesoporous TiO_2-Sn/C core-shell nanowire arrays, where Sn formed by a reduction of SnO_2 was encapsulated into TiO_2 nanowires with carbon coating (Figure 5). The resulting TiO_2-Sn/C nanowire arrays displayed rechargeable discharge capacities of 769, 663, 365, 193, and 90 mA h g^{-1} at 0.1 C, 0.5 C, 2 C 10 C, and 30 C, respectively (1 C = 335 mA g^{-1}). The TiO_2-Sn/C nanowire arrays exhibit a capacity retention rate of 84.8% with a discharge capacity of over 160 mAh g^{-1} , even after 100 cycles at a high current rate of 10 C [28].
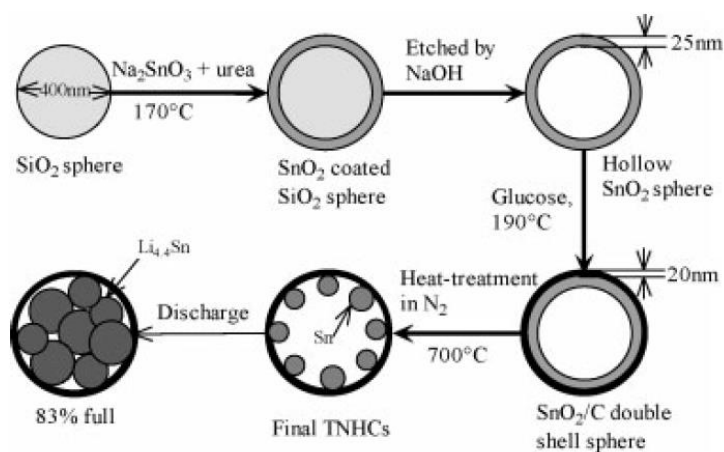
Figure 4 Synthetic scheme of tin nanoparticles encapsulated in elastic hollow carbon spheres (TNHCs) [27].
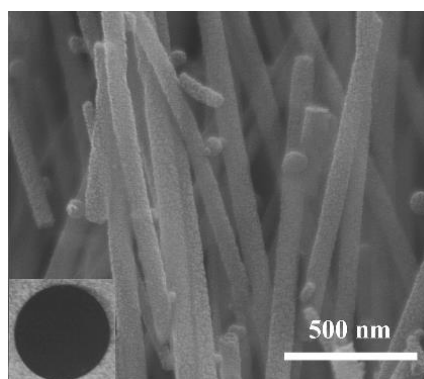
Figure 5 SEM images of the prepared nanowire arrays of TiO2-Sn/C. [28]

In order to overcome the issues of Sn-based materials mentioned above, particularly results from Zhang et al. [27] and Liao et al. [28], we propose a cost-effective and simple method to prepare core-shell Sn/Ti anode materials that show better electrochemical

performance than simple Sn/Ti mixture materials and porous Sn materials.

3. Experimental

3.1. Materials

Materials used for the experiments are listed in Table 2.

Table 2 Main Materials used in the experiments.

Materials	Vendor	Chemical formula
Tin(II) chloride dihydrate	Alfa Aesar	$SnCl_2 \cdot 2H_2O$
Sodium Carbonate	VWR	Na_2CO_3
Calcium chloride dihydrate	Alfa Aesar	$CaCl_2 \cdot 2H_2O$
Titanium(IV) isopropoxide	Alfa Aesar	$C_{12}H_{28}O_4Ti$
Poly(acrylic acid)	Alfa Aesar	$[-CH_2CH(CO_2H)-]$
Separator	Celgard	PP/PE/PP
CMC		Carboxy Methylated Cellulose
SBR		Styrene-butadiene rubber
Electrolyte		EC/EMC+5%FEC+1%VC
Carbon black		C

3.2 Synthesis of Materials

A certain amount of $SnCl_2 \cdot 2H_2O$, $NaCO_3$ and $CaCl_2 \cdot 2H_2O$ was dissolved in de-ionized (DI) water to make the concentrations as 0.025, 0.5, 0.3 mol L^{-1}, respectively. In order to compare the difference ratio of the Sn and Ca effect on the performance of the electrode materials, several control samples were prepared. The concentration of $SnCl_2 \cdot 2H_2O$ of these controls were 0.025, 0.05 and 0.06 mol L^{-1}, ceteris paribus. And the concentration of $CaCl_2 \cdot 2H_2O$ were 0.3 and 0.36 mol L^{-1}, all other variables were same. The $SnCl_2$ and the $NaCO_3$ solutions were mixed while stirring by a magnetic

stirring bar for 5 min at 300 rpm, followed by adding the $CaCl_2$ solution while stirring

at 300 rpm for 20 minutes, resulting in a white suspension. According to the reference

[36], chemical equations of the above process are shown in (5) & (6).

$$6SnCl_2 + 6Na_2CO_3 + 2H_2O \rightarrow Sn_6O_4(OH)_4 + 12NaCl + 6CO_2\uparrow \qquad (5)$$

$$Na_2CO_3 + CaCl_2 \rightarrow CaCO_3 + 2NaCl \qquad\qquad\qquad (6)$$
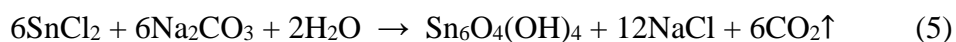
After filtration, the resulting white precipitate was dried at 80 °C for 4 h under

vacuum. The vacuum filter flask is shown in Figure 6.
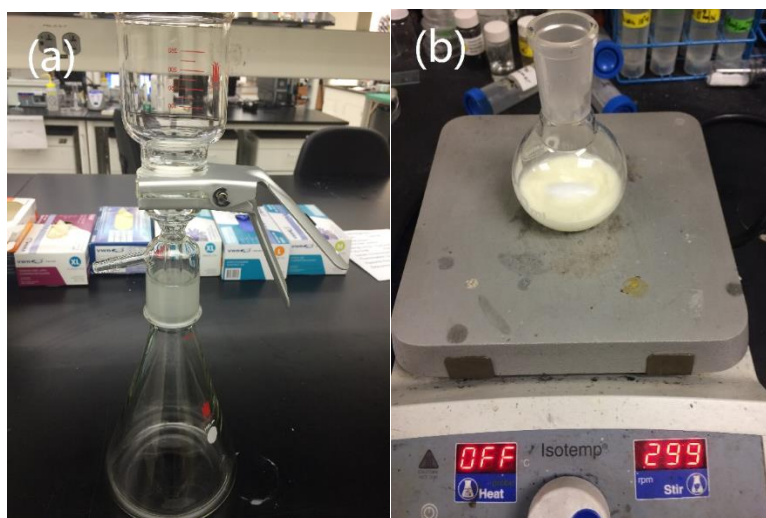
Figure 6(a).Filter flask. (b). Stirring samples on magnetic stirrers.

With gentle grinding, the fine powder was transferred into a flask, containing 10 ml

ethyl alcohol. In order to compare the different ratio of the Ti effect on the structure and

performance of the materials, various amounts of titanium isopropoxide (TIPT) were

prepared to make controls. The molar quantities of controls are 0.0028, 0.0035 and

0.0042 mol, ceteris paribus, which will be detailed later. Weighted TIPT was slowly

dropped into the flask.

To make the hydrolysis homogenous, we premade the alcohol at a volume ratio of

(ethyl alcohol: DI water) 4.5ml: 0.5ml, 2ml: 0.5ml and 0.5ml: 0.5ml, then added the alcoholic solution into the flask dropwise, followed by adding 5 ml DI water and stirring at 300 rpm for 10 min to hydrolyze completely. The turbid liquid became a faint yellow. The stirring process was shown in Figure 5(b). The chemical equation of the above process was shown in (7).

$$Ti\{OCH(CH_3)_2\}_4 + 2\ H_2O \rightarrow TiO_2 + 4\ (CH_3)_2CHOH \qquad (7)$$
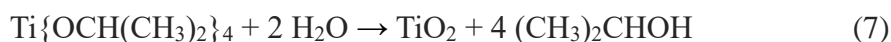
A light yellow paste product was obtained after filtration and was dried under vacuum at 80°C for 4 h. The resulting powders were observed by SEM, exhibiting a shell-core structure, as indicated by the crushed particles (Figure 7).
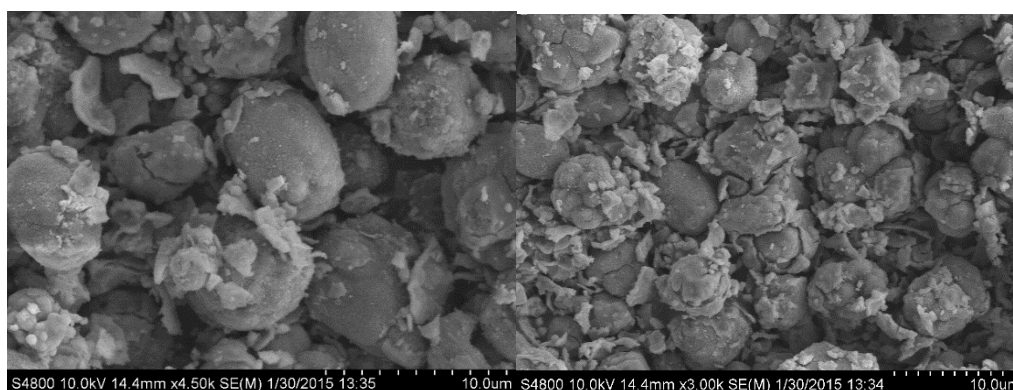
Figure 7 SEM images of prepared samples before removing the CaCO$_3$, which appeared from split shell.

Figure 8(a). Tube furnace (Thermo Scientific Lindberg/Blue M™ Vacuum Ovens). (b). Samples became white powder after calcination

A crucible with powder was put into the tube furnace, as shown in Figure 8(a), and heated at 500 °C for 20 min for crystallization. The white powder in Figure 8(b) is the product after heat treatment.

The resulting white powder was then put into 100 ml DI water and stirred at 300 rpm and then dropped in dilute hydrochloric acid to remove the $CaCO_3$. Additional stirring was applied for 20 min to ensure the complete reaction.

A vacuum filter flask was used to filter the turbid liquid, followed by rinsing using DI water until the acid was completely gone.
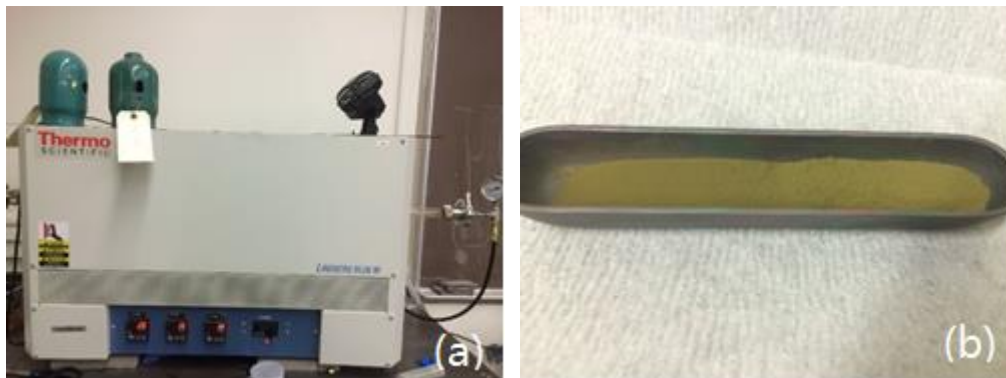
Figure 9(a). Vacuum tube oven. (b). Earthy yellow powder obtained after reduction.

After drying by vacuum oven at 80 °C for 4 h, the sample was ground into powders. The powders with the crucible were then put into the vacuum tube oven shown in Figure 9(a), to allow SnO_2 to be reduced to Sn under a hydrogen atmosphere at 500 °C for 1 h. The final product in Figure 9(b) was sealed in a glass bottle.

3.3. Battery assembly

The active material, carbon black, and binder were mixed by a mass ratio of 8:1:1. In order to compare the different binder effects of the performance of material, two

kinds of water-based binder (CMC-SBR and PAA) were used. The mixture was uniformly ground with an appropriate viscosity and coated on the cleaned Cu foil (Figure 10).
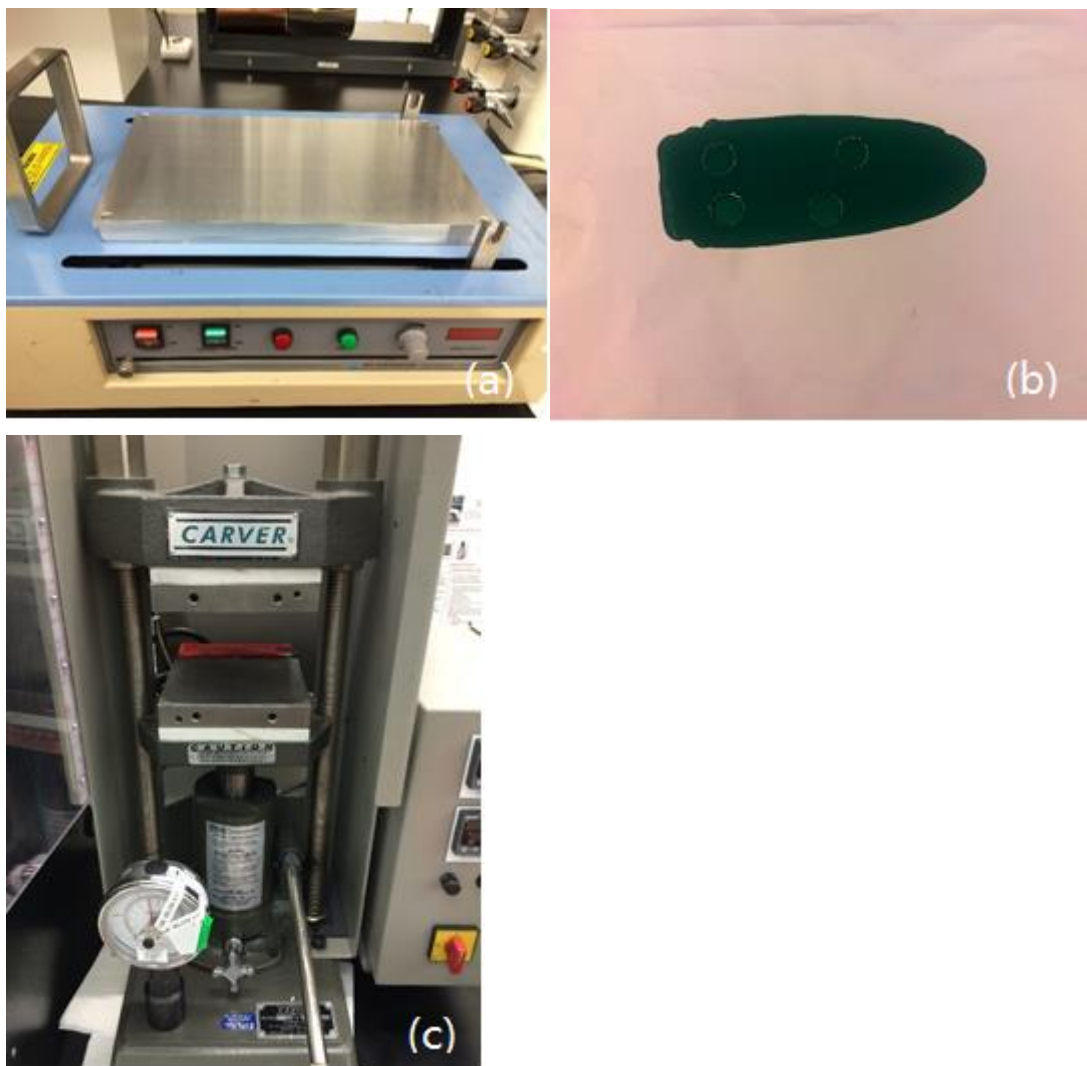
Figure 10(a) (b). Active materials coat on Cu foil. (c). Tablet press.

The slurry-coated copper foil was dried in a vacuum oven at 80 °C for 12 h, followed by being bunched into electrode slices that had a diameter of 7/16 in, and then pressed at 4 T. A tablet press shown in Figure 10(c) was used for tableting the slices for assembly.
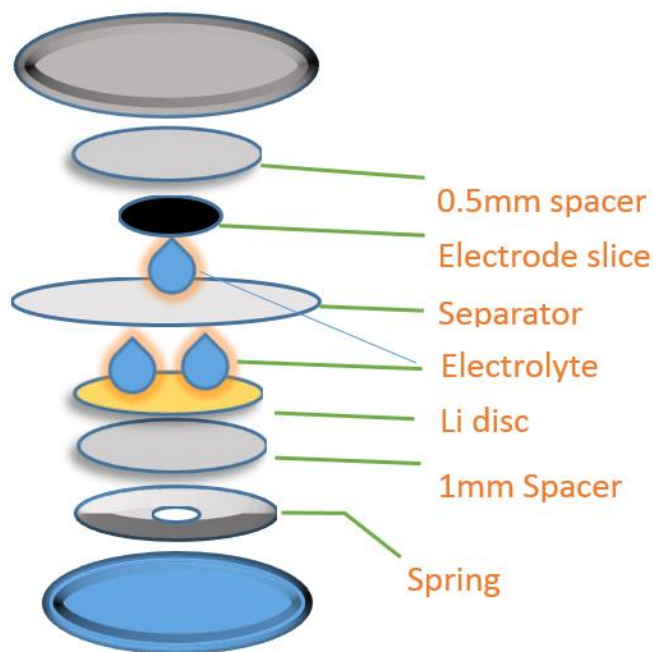
Figure 11 CR2032 cell battery assembly diagram.

Figure 12(a). Glove box. (b). Hohson Corp HS-HCR2 manual coin crimper in glove box.

Batteries were assembled in a glove box (Figure 12(a)) that was filled with argon and crimped by a HS-HCR2 manual coin crimper presented in Figure 12(b). Oxygen and moisture contents were less than 0.5 and 0.1 ppm, respectively. A Lithium disk was used as the counter electrode. 5% Fluoroethylene Carbonate (FEC) and 1% Vinylene

Carbonate (VC) were used as electrolyte additives. A schematic illustration of assembling is shown in Figure 11.

3.4. Material Characterization

1. Phase analysis

The phase of sample was analyzed by X-Ray Diffraction (XRD) (Bruker D8 Discover), which is presented in Figure 13(a), using Cu-Kα as a radiation source from 10° to 70° with a step size of 0.02°.

2. Morphology and composition analysis

The morphology of samples was observed by a scanning electron microscope (SEM) at an acceleration voltage of 10 kV. Energy-dispersive X-ray spectroscopy (EDS) was used to characterize the elemental composition. SEM was carried out with a Hitachi S-4800 electron microscope.

3. The structures were analyzed by Raman spectroscopy (Renishaw 1000B) (Figure 13(d)).

4. The surface chemical composition was characterized by using XPS (Perkin Elmer 5440 X-Ray Photoelectron Spectrometer) that is shown in Figure 13(e). The binding energy of C 1s equal to 284.8 eV as a benchmark for the binding energy correction.

5. Surface area and pore size of powders measured by BET (Micromiritics ASAP 2020) are shown in Figure 13(c).

6. Cyclic voltammetry (CV) and electrochemical impedance spectroscopy (EIS) of the as-prepared anodes were measured on a PARSTAT 4000 electrochemical station by

using a three-electrode cell, with the Sn/C composite electrode as a working electrode,

a Lithium disk as a counter electrode, and a Lithium ring as a reference electrode. CV

was carried out at a scanning rate of 0.05 mV s^{-1} while EIS was tested between 10,000-

0.1 Hz with an amplitude of 10 mV.

Figure 13(a). Bruker X-Ray Diffraction (b). Land battery testing system. (c). Micromiritics ASAP 2020 BET measurement. (d). Raman spectroscopy (Renishaw 1000B). (e). Perkin Elemer 5440 X-Ray Photoelectron Spectrometer.

3.5 Characterization of the Electrochemical Performance

A galvanostatic charge-discharge test was carried out on a land battery testing system. The specific current densities and specific capacities were calculated based on the total mass of the active materials. Cyclic voltammetry (CV) started with the open circuit voltage of approximately 3 V, while scanning between 10 mV and 3 V, at a scan rate of 0.05 mV s^{-1}. All tests were carried out under room temperature.

4 Structure and Performance Results

4.1 Structure Characterization

SEM

Morphology of the materials after being reduced was observed by SEM. Compared with the materials before removing the template (Figure 7), the shell structure of the final product can be best seen under SEM, which is composed of TiO_2. Figure 14 displays the morphology of various samples. We can find hundreds nanoparticles anchored on the inner surfaces of TiO_2 shells. By using EDS, Sn was concentrated in these nanoparticles. The typical size of TiO_2 sphere and Sn particles are 5-8 μm and 50-250 nm. This kind of hollow sphere structure that we designed can supply a huge buffering space for the volume expansion of Sn during charge and discharge. At the same time, nanocrystallization of Sn can also enhance the cycle performance of the

materials.
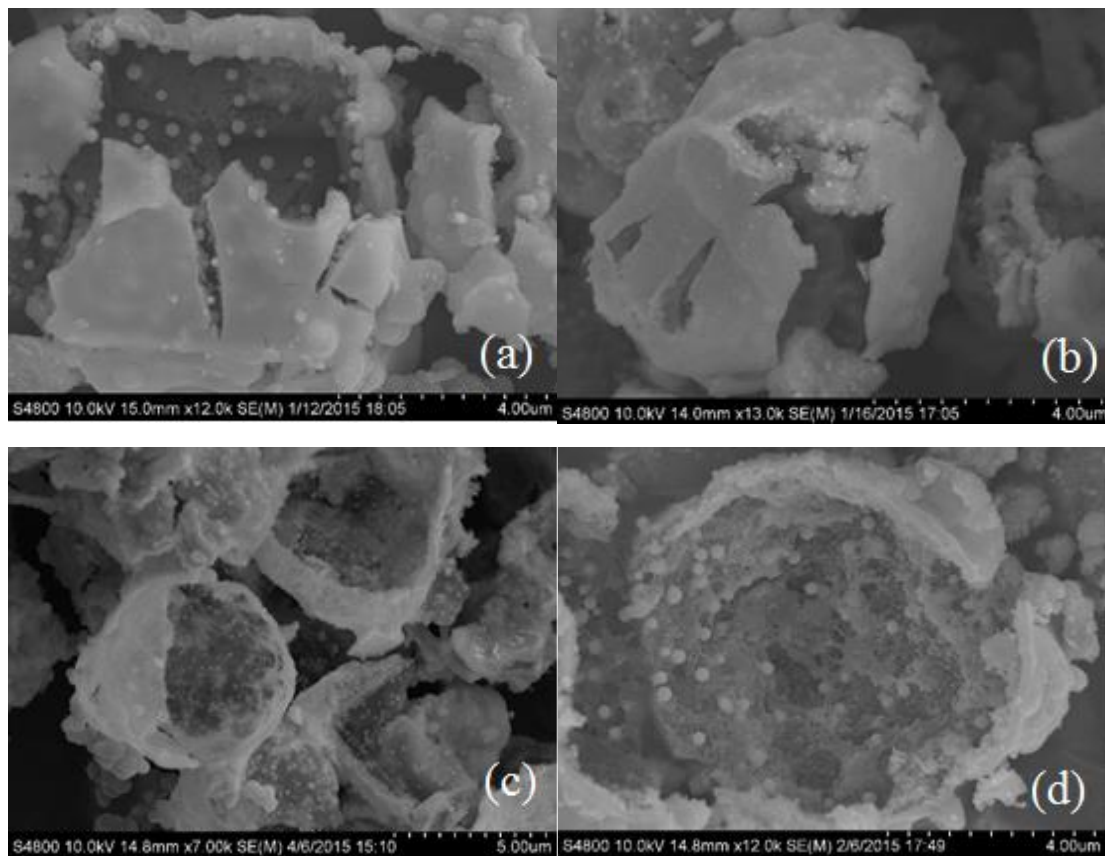
Figure 14 Microstructure of samples observed by scanning electron microscopy (SEM). The full view of TiO_2 sphere can be observed in (b) and (c). The Sn particles can be clearly found in (a) and (d).

XRD

XRD results are given in Figure 15. The XRD peaks of the three samples were indexed (200), (101), (220), (211), (301), (112) and (321) planes of Sn (JCPDS No. 04-0673). The peaks of TiO_2 are not clearly found by XRD, likely due to the formation of $(Ti+Sn)O_2$ solid solution [35] during the process of heat treatment, resulting in shifting of the peak of TiO_2 in the XRD pattern. The existence of Ti can be proved by XPS, Raman and SEM-EDS results.

The XRD patterns for three samples in various batches we obtained are very similar,

and no contaminants were detected, especially $CaCO_3$ or other calcium compounds. It

suggests that our products of different batches are consistent and reliable.
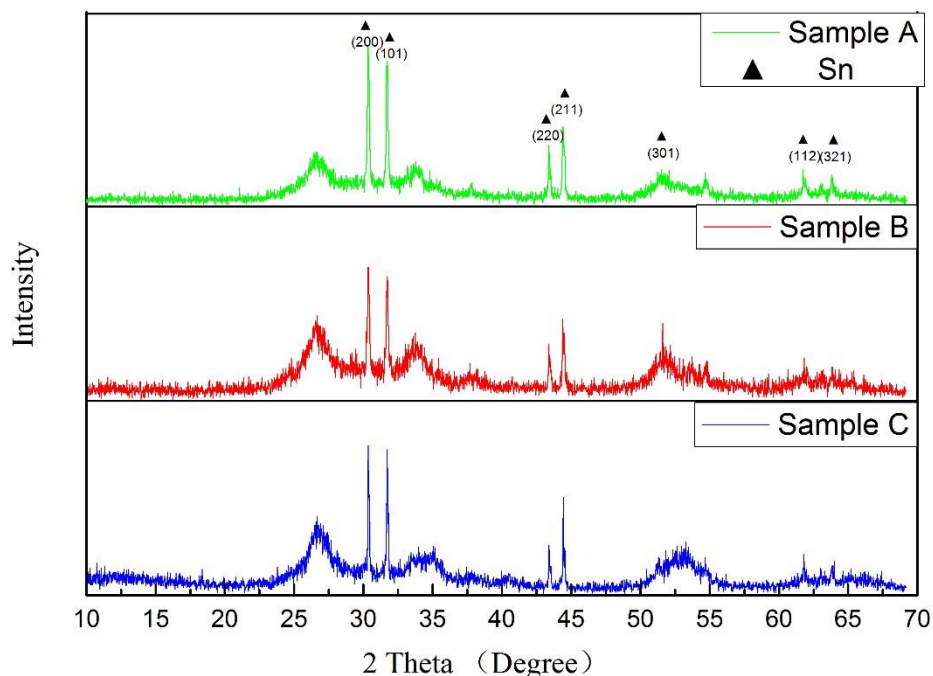
Figure 15 XRD spectra of samples from various batches.

Raman

Figure 16 shows a representative Raman spectrum of the samples. Raman

spectroscopy relies on Raman scattering of monochromatic light usually from a laser.

The laser light interacts with molecular vibrations, phonons or other excitations in the

system, resulting in the energy of the laser photons being shifted up or down. The shift

in energy provides a fingerprint by which molecules can be identified, which can help

us to confirm the TiO_2 in our composite. Similar results were obtained from several

other different samples. According to the reference[37], Raman active modes for anatase

TiO_2 could be detected at 139, 194, 395, 514 and 634 cm^{-1}, while peaks for our materials

appeared at 105, 163, 418 and 608 cm^{-1}. The consistent peak shift toward a lower

wavenumber suggests the presence of a Sn/TiO$_2$ solid solution.
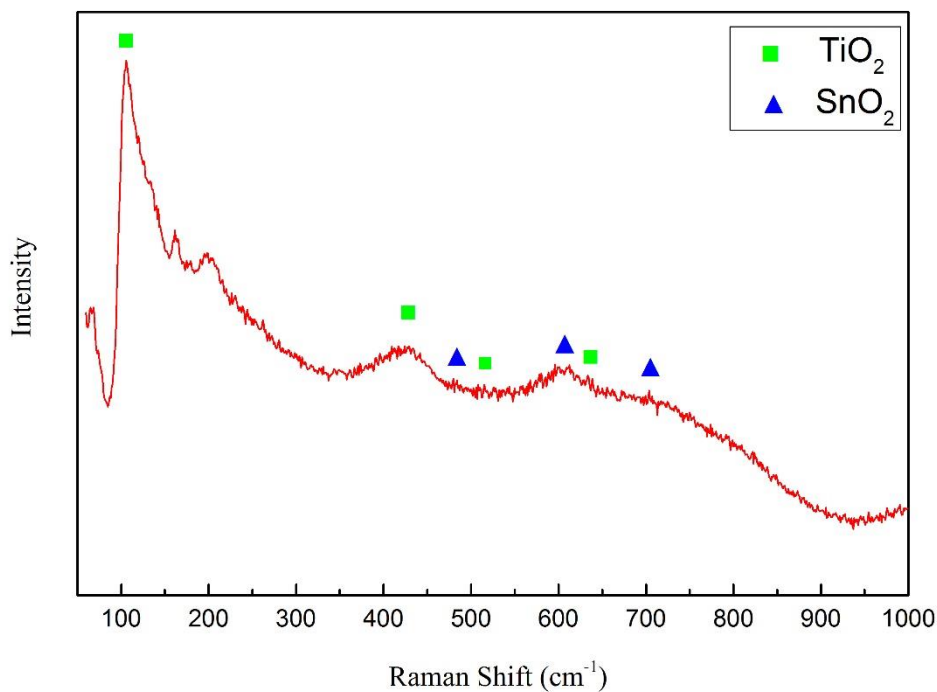
Figure 16 Representative Raman spectrum of the samples.

XPS

According to the reference [33], the binding energy of the Ti^{+4} (TiO$_2$), Ti^{3+} (Ti$_2$O$_3$) and

Ti^{2+} (TiO) are 458.7eV, 456.8 eV and 455.2 eV, respectively. Accordingly, all Ti was

distributed on Ti^{+4} (TiO$_2$).

From the Sn 3d, we can find the peak at 486.5 eV (Figure 17 & 18) is close to Sn

3d$_{5/2}$ SnO$_2$ (487.3 eV) and SnO (487.0 eV), but far away from that of Sn (495.3 eV).

This suggests that the Sn in our composite is covered by SnO$_x$ because Sn is naturally

easily oxidized [36].
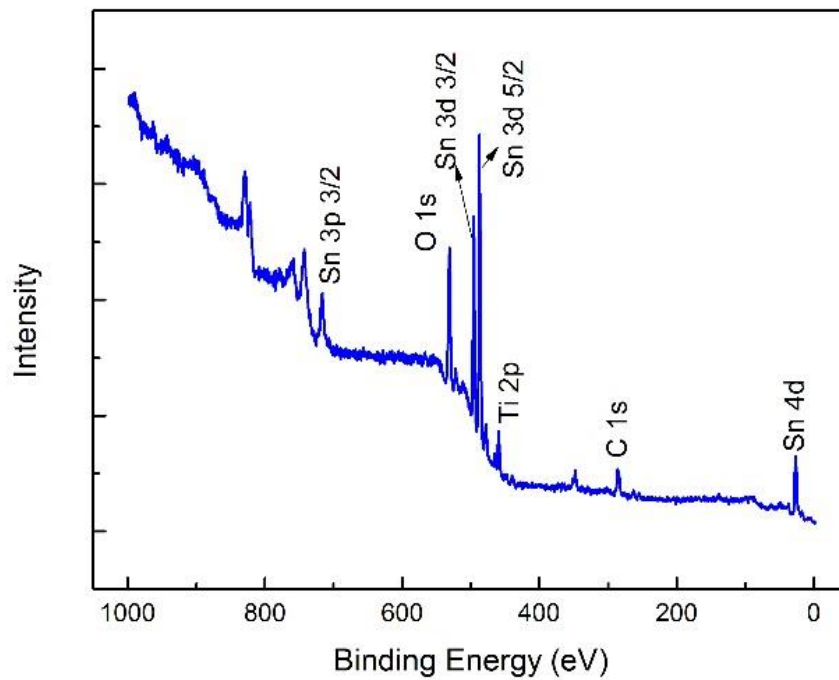
Figure 17 Overview of XPS result.
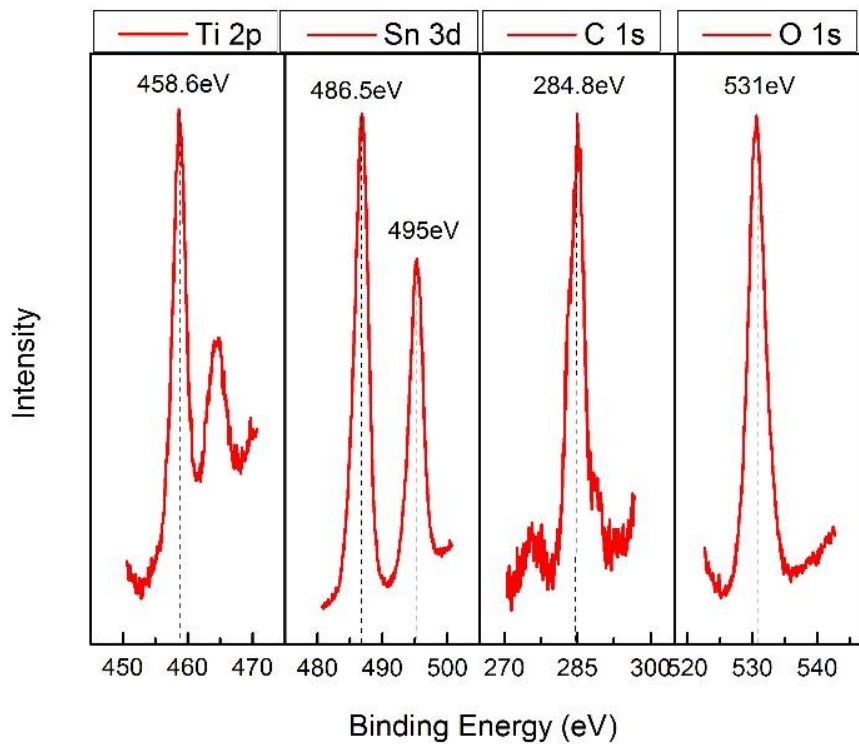
Figure 18 Individual XPS peak of Ti, Sn, C and O.

BET

According to the BET results, the specific surface area is 29.5 m² g^{-1}, with the relatively low surface area ascribed to the high density of Sn. Figure 19 shows BJH adsorption dA/dlog (D) pore volume, indicating that pores are present in materials, and the diameter of pores is mainly distributed between 5 nm to 10 nm.
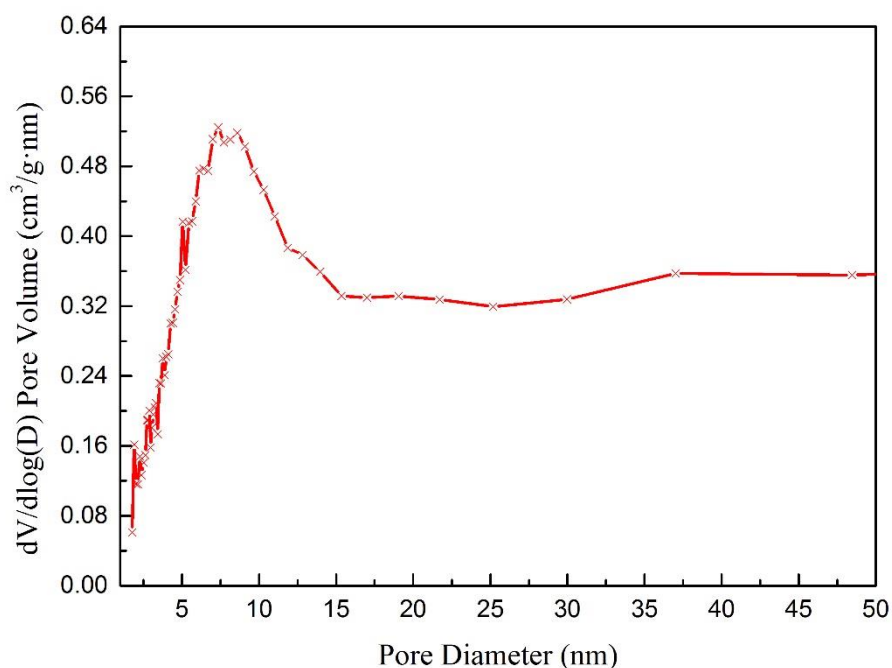
Figure 19 Pore size distribution according to the BJH adsorption branch.

4.2 Electrochemical performance

4.2.1 The first Charge-Discharge performance

The specific capacity of the first charge of the tin/TiO$_2$ composite is 698 mAh g^{-1}, and the first irreversible capacity is 312.8 mAh g^{-1}, with a Coulombic efficiency of 69 %

(Figure 20). The Coulombic efficiency of the composite is related to some irreversible

processes such as SEI formation and the reduction of surface SnO_x. There is no apparent

discharge plateau below 0.6 V for all samples. In the subsequent charge curve, a charge

plateau around 0.5 V corresponds to the de-alloying process of Li-Sn. For the alloying

and de-alloying of SnO_2, according to the previous reports, the chemical reaction is:

$$SnO_2 + 4Li^+ + 4e^- \rightarrow 2Li_2O + Sn \qquad (7)$$
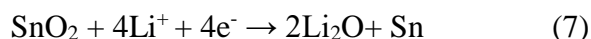
According to the literature, there should be a charge plateau around 0.9 V in a charge

curve. However, it was not found in our charge-discharge figure, indicating that SnO_2

is not the main composition in our materials. Most Sn exists as an elemental Sn that can

enhance the first cycle performance.
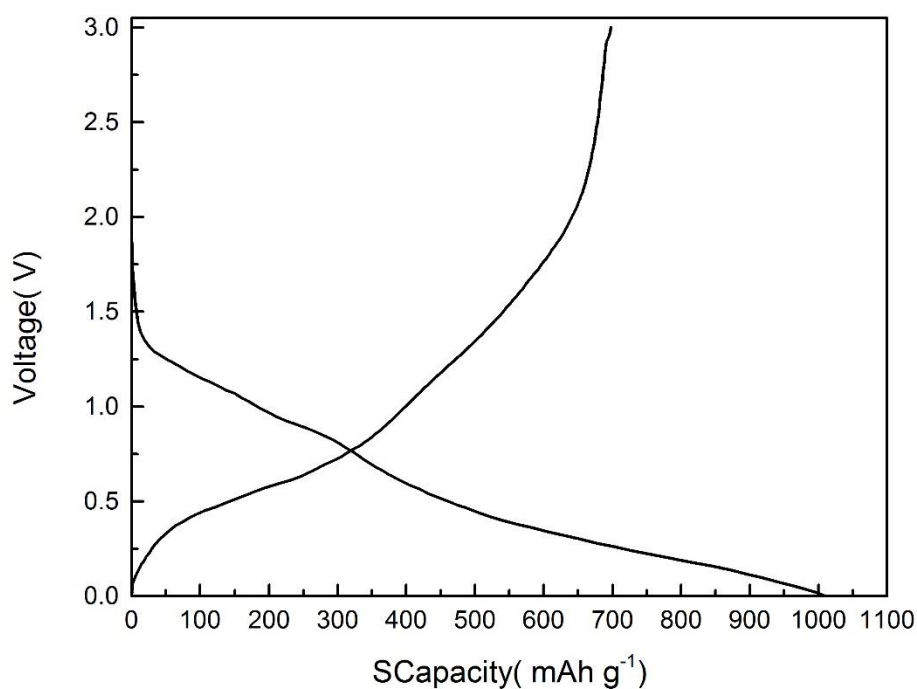
Figure 20 Specific capacity of first cycle.

4.2.2 Cyclic Voltammetry

Figure 20 shows the initial three CV cycles of the Sn/TiO$_2$ materials. A high irreversible reduction peak appeared in the process, which indicates the formation of the SEI film. A reduction peak also is found between 0.1-0.25 V, corresponding with an oxidation peak around 0.5 V, which indicates the reversible alloying-dealloying process of Li-Sn. The Li$^+$ intercalation and deintercalation process is also shown from the reduction peak at 1.0 V and the oxidation peak at 1.25 V. Compared with the second and third cycle, we can find a reduction peak around 0.75 V, which is considered to be the main reason for the first cycle reversibility.
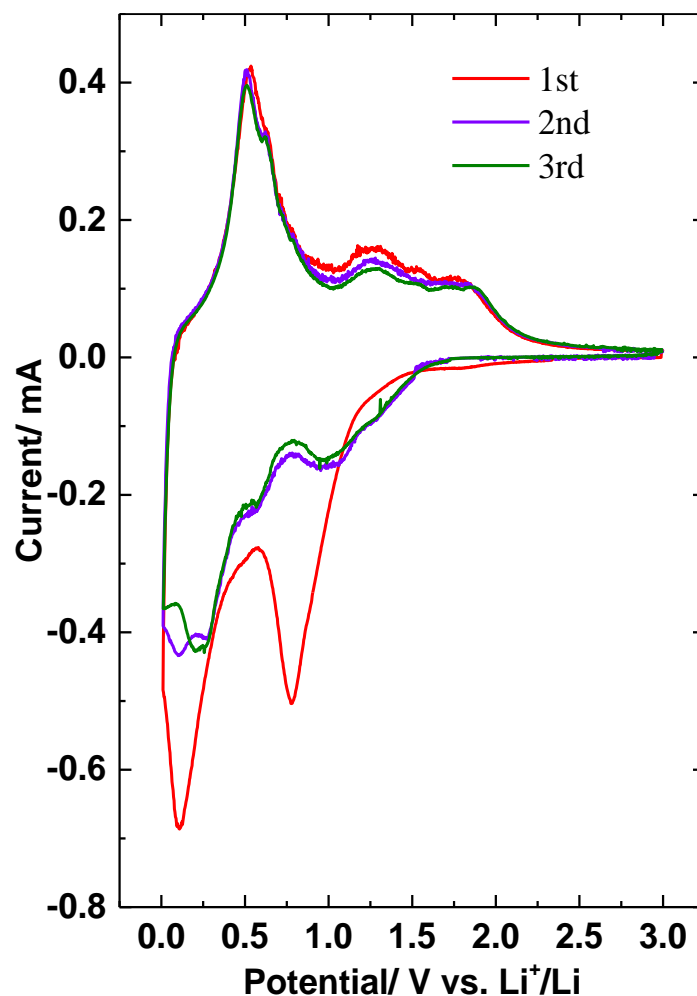
Figure 21 First three cycles of cyclic voltammogram of materials.

4.2.3 Electrochemical impedance spectra (EIS)

Figure 22 depicts the electrochemical impedance spectra (EIS) of the tin/TiO$_2$ composite in 2 h, 4 h, 6 h, and 8 h, in fully charged and fully discharged states. The equivalent circuit for fitting the Nyquist plots (using ZView) and the corresponding parameters of elements are shown in Figure 23 and Table 3. Fitting results of a fully discharged battery are based on the equivalent circuit A because only one semi-circle can be observed and there is no charge transfer resistance due to the high potential. The parameter of diffusion process is shown as W, which cannot be found in the fully charged curve based on the equivalent circuit C because no diffusion resistance is present. The Ohmic resistance was measured by the intercepts of the Nyquist plots at high frequencies; the values are 2.6 Ohm for fully charged and discharged states and 2.2, 2.4, 2.4, 2.4 Ohm for 2, 4, 6, and 8 h charged states at C/10, respectively (Shown as R$_1$ in Figure 23, which is determined by the intersection of the curve and X axis in Figure 22). The EIS spectrum obtained from charged states consists of two depressed semi-circles, resulting from the SEI layer and the charge transfer process (Shown as R$_2$ and R$_3$ in C of Figure 23, determined by diameter of first and second semi-circles of curves in Figure 22, respectively). The measured resistances are 25.1 and 104.1 Ohm for the SEI layer and the charge transfer process, and the fitting errors are 0.6 and 0.4 %, respectively. We related the depressed semi-circle at high frequencies to the SEI layer because we can also find it in the fully discharged curve due to the initial charge cycle; its resistance is 12.2 Ohm, which is a little higher than the resistances of 2, 4, 6, and 8 h charged states but lower than that at the fully charged state.
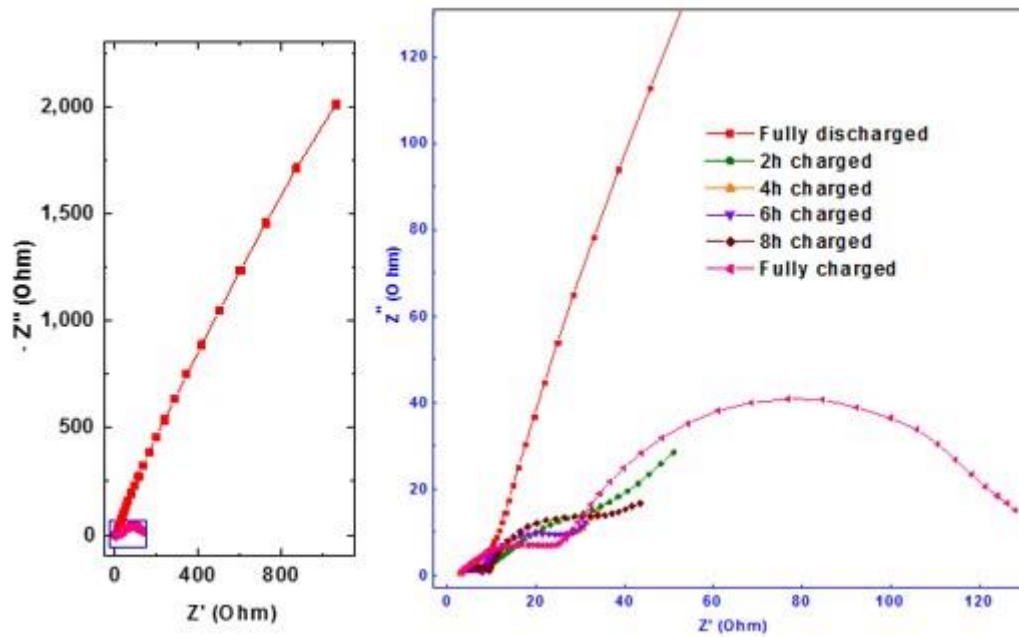
Figure 22 Nyquist plots of materials at 2 h, 4 h, 6 h, and 8 h, fully charged and fully discharged states.
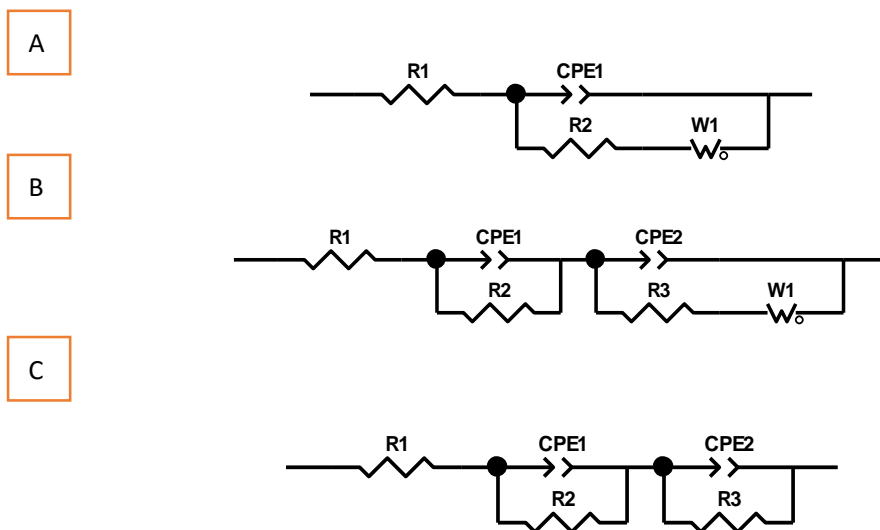
Figure 23 Equivalent circuits of fully discharged (A), partially charged (B), and fully charged (C) state.

Table 3 Corresponding parameter of elements in equivalent circuits

Charge state	R1	R1 (Error %)	R2	R2 (Error %)	R3	R3 (Error %)
Fully discharged	2.6	1.4	12.2	3.0	N/A	N/A
2h charged	2.2	2.7	9.1	5.7	24.7	63.0
4 h charged	2.4	1.8	7.0	1.4	12.7	4.6
6 h charged	2.4	2.0	6.2	1.4	13.5	4.2
8h charged	2.4	2.1	7.7	1.4	21.4	8.4
Fully charged	2.6	0.7	25.1	0.6	104.1	0.4

Charge state	W1-R	W1-R (Error %)	Equivalent circuit
Fully discharged	41581.0	5.6	A
2h charged	28.6	128.7	B
4 h charged	25.0	10.3	B
6 h charged	25.3	8.4	B
8h charged	45.5	5.6	B
Fully charged	N/A	N/A	C

4.2.4 Cycle stability

Due to the huge volume expansion of Sn in Li^+ intercalation and deintercalation process, the structure of Sn is easy to collapse, resulting in rapid decay of the reversible capacity [34].

In our design, TiO_2 shell offers a huge buffer space for the volume expansion of Sn during charge and discharge. At the same time, nanocrystallization of a Sn particle can also maintain a good electrical contact, so our materials showed excellent cycle stability. As shown in Figure 24, the specific capacity of samples can be retained above 450 mAh g^{-1} at 100 cycles and 400 mAh g^{-1} at 200 cycles.

The capacity dropped relatively quickly in the first few cycles, but became stable after 10 cycles (Cells were cycled at C/20 for 2 cycles and then at C/5 for 200 cycles). Compared with the first reversible specific capacity 498.5 mAh g^{-1}, the specific capacity of our product can maintain 95.3% at 100 cycles and 78.8% at 200 cycles.

The initial discharge (delithiation) capacity at 0.05 C is 698 mAh g^{-1} (Figure 25), which is very close to the theoretical capacity of Sn/TiO_2 materials. Sn and TiO_2 contributes to 551.6 and 146.3 mAh g^{-1}, respectively (The molar ratio of Sn/TiO_2 is 0.857 and the mass ratio is 1.274; theoretical capacities of Sn and TiO_2 are 993 and 335 mAh g^{-1}, and thus the theoretical capacity of the composite material is 703.3 mAh g^{-1}). After activation for the initial two cycles, the anode was cycled at 0.2 C, exhibiting capacities of 498.5 and 393.2 mAh g^{-1} for the 4th and 200th cycles, respectively. By comparing with the results in the reference [36], we can conclude that the capacity located above 0.9 V mainly resulted from TiO_2.
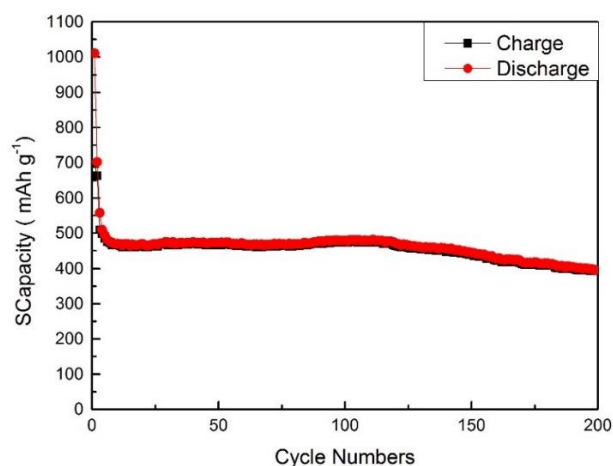
Figure 24 Specific capacity of sample in 200 cycles.
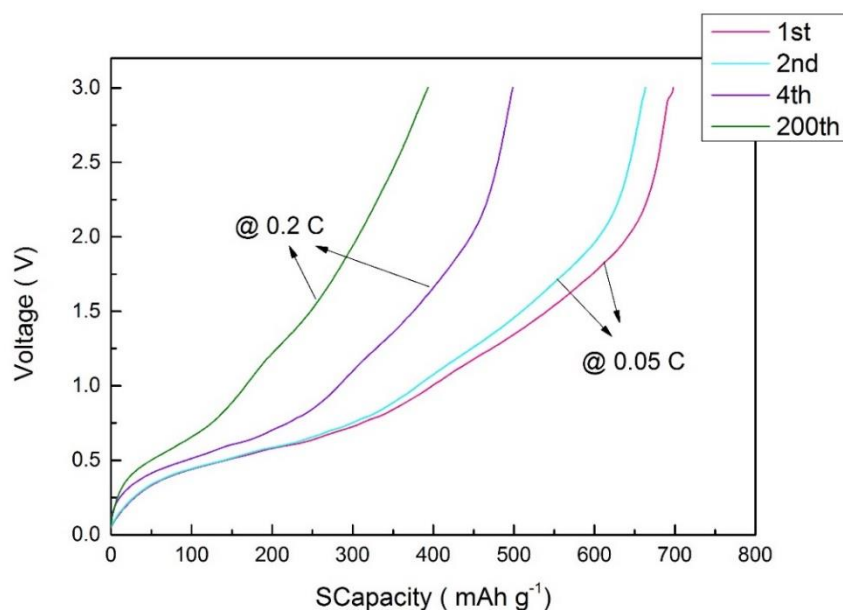
Figure 25 Charge Curve of the 1st, 2nd, 4th and 200th cycles.

4.2.5 Rate performance

The rate performance of our materials is shown Figure 26. At a high current density of 2C, the capacity can reach 231 mAh g^{-1}, 40% of the capacity obtained at the small current of 0.1C (567 mAh g^{-1}). It is worth mentioning that the capacity of this anode material can reach 311.6 mAh g^{-1} at 1C.
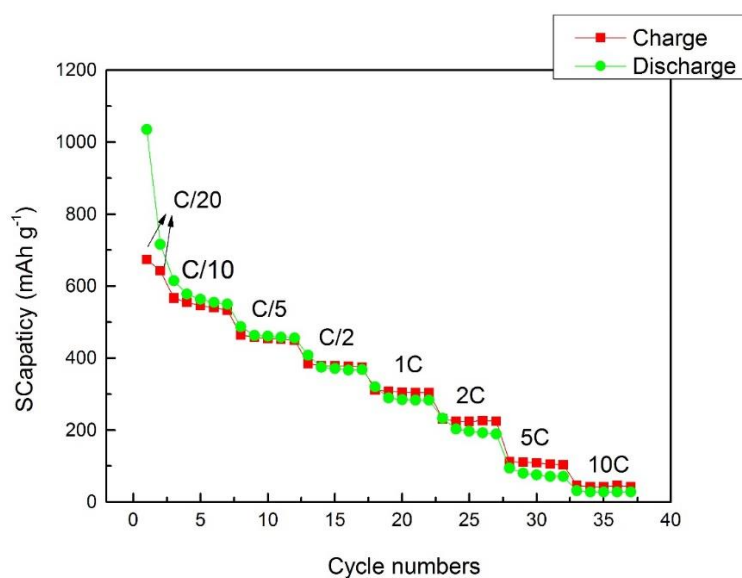
Figure 26 Specific capacity of materials at various C rates (1C=600 mA g^{-1}).

5 Parametric Studies

5.1 Binder impact on performance

Poly (acrylic acid) (PAA) is the most suitable binder compared with NMP and CMC-SBR. To compare the binder effect on the performance of material, some control tests were conducted. We found that the capacities of batteries that used NMP and CMC-SBR as a binder dropped rapidly after 100 cycles, possibly because of the destroyed structure.

5.2 Effect of Sn content on performance

In order to compare the different ratios of Sn on the performance of the electrode materials, several controls were prepared. The molar mass of $SnCl_2$ of these controls are 0.00125, 0.0025 and 0.003 mol, ceteris paribus. As can be seen in Figure 27, the XRD peak intensity of Sn peak of 0.0025 mol L^{-1} sample is significantly higher than that in the case of the 0.00125 mol L^{-1}.
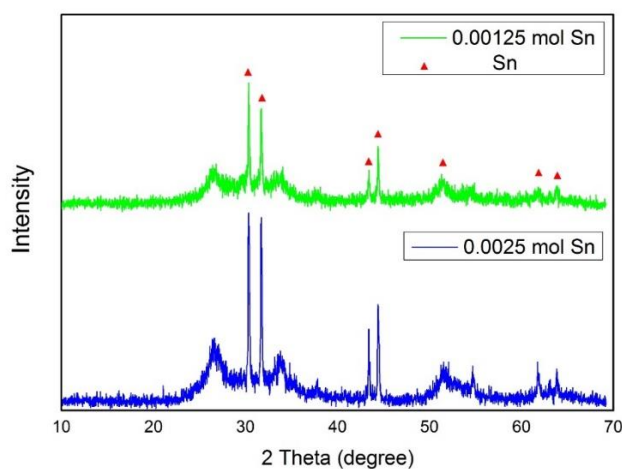
Figure 27 XRD diagram of samples containing 0.00125 and 0.0025 mol Sn.
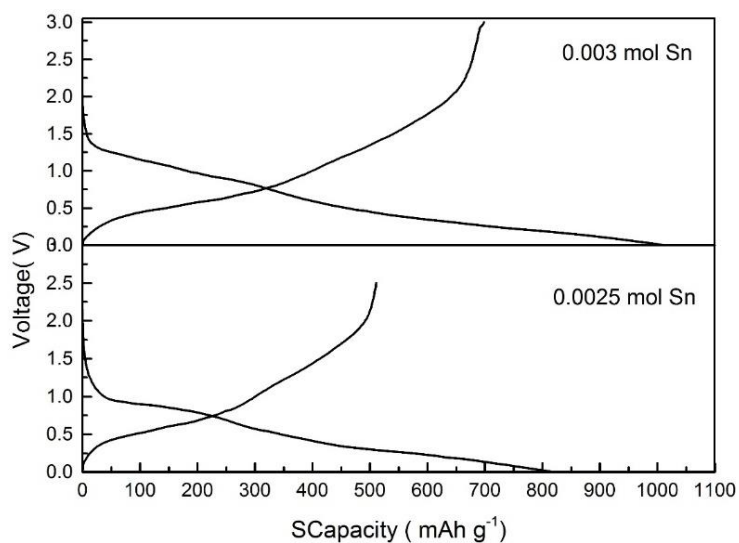
Figure 28 Specific capacity of first cycle of samples containing 0.003 and 0.0025 mol Sn, respectively.

Figure 28 shows the first charge-discharge property of the different Sn content samples. The first charge capacities are 510.9 mAh g^{-1} and 698 mAh g^{-1} for 0.0025, and 0.003 mol $SnCl_2 \cdot H_2O$ samples, respectively. The first irreversible capacity and first cycle Coulombic efficiency are 303.1 mAh g^{-1} and 312.8 mAh g^{-1}, 62.8% and 69%, respectively. Obviously, a higher Sn content resulted in a better first charge capacity and first cycle Coulombic efficiency.
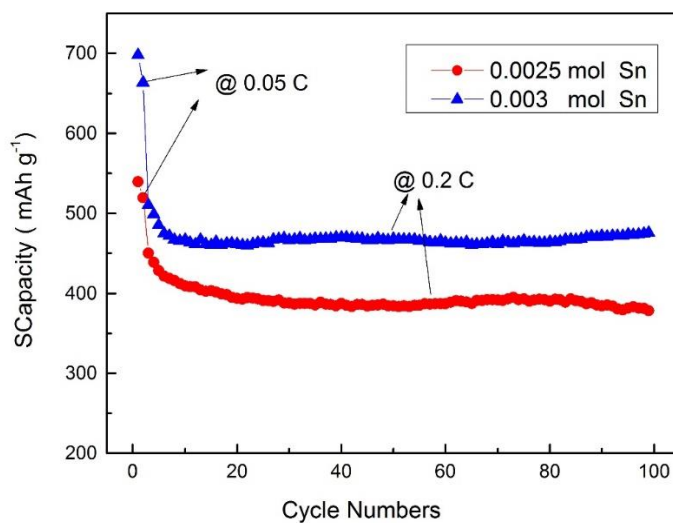
Figure 29 Specific capacity in 100 cycles of three samples content Sn 0.0025 and 0.003, respectively.

Figure 29 shows the specific capacity in 100 cycles for three different Sn contents. The sample obtained with 0.003 mol and 0.0025 mol $SnCl_2 \cdot H_2O$ can retain the specific capacity 460 mAh g^{-1} and 400 mAh g^{-1} at 100 cycles, respectively.

5.3 The effects of different Ti content

In order to compare the effect of the different Ti content on the structure and performance of the materials, several controls were prepared. The molar quantities of TIPT of controls were 0.0028, 0.0035, and 0.0042 mol, ceteris paribus.

5.3.1 Effect of Ti content on structure

Considering that $CaCO_3$ is the template for TiO_2 shell, TiO_2 is stretched over the $CaCO_3$ sphere before it is removed. Supposing that the size of $CaCO_3$ spheres is homogenous on the same condition, the thickness of shell will be mainly determined by the amount of the Ti. In Figure 28, the molar quantities of TIPT of (a), (b) and (c) are 0.0042, 0.0035 and 0.0028 mol, respectively. Obviously, the TiO_2 shell in Figure 29(a) is thicker than the others, while maintaining a more complete hollow sphere structure. On the contrary, we can hardly recognize the shell structure of the sample in Figure 29(c); it just tore to pieces.

As a result, we can infer, in the same condition, the sample with higher molar quantities of Ti tends to form a thicker TiO_2 and has a higher possibility of maintaining the original structure.
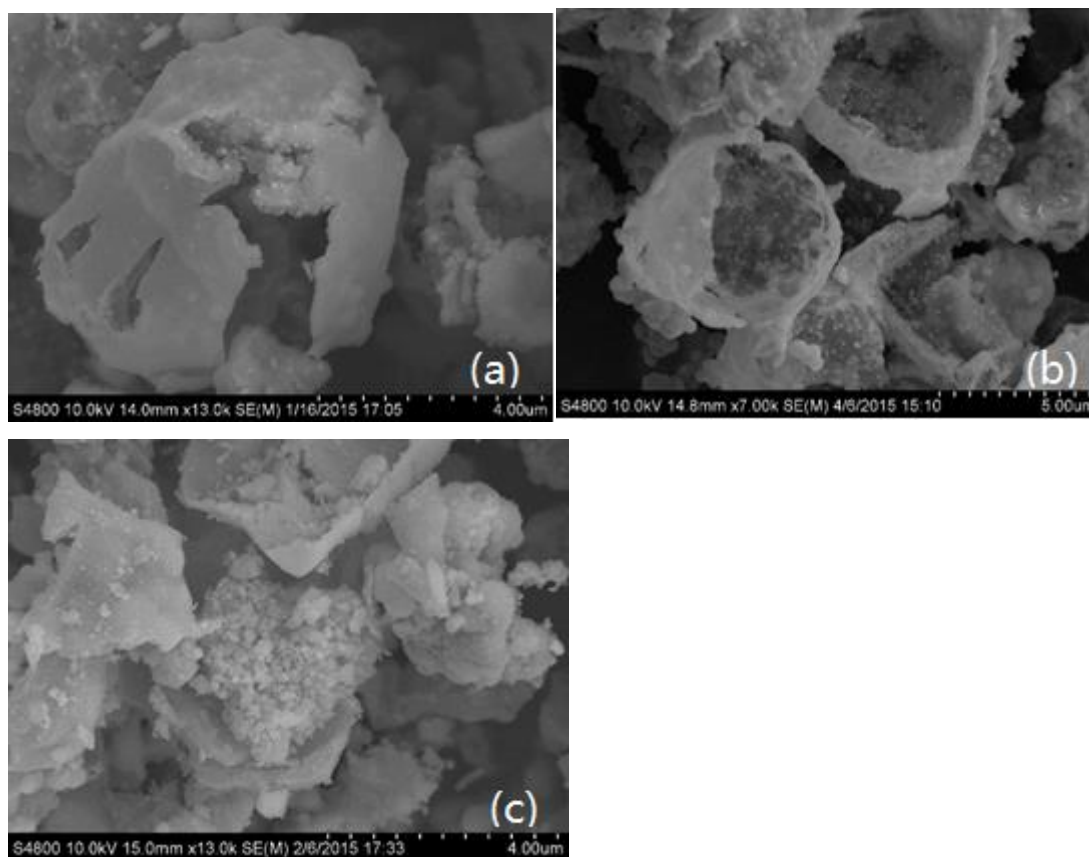
Figure 30 SEM of samples (a), (b) and (c) with 0.0042, 0.0035 and 0.0028 mol TIPT (which indicate 0.0028, 0.0035 and 0.0042 mol of Ti Content, respectively)

5.3.2 Ti content impact on electrochemistry

The electrochemical properties of materials obtained in the presence of 0.0028, 0.0035, and 0.0042 mol TIPT are shown in Figure 29. The first charge capacities of the samples in the case of 0.0028, 0.0035, and 0.0042 mol TIPT content samples are 650, 550, and 540 mAh g^{-1}; and the first reversible capacities are 620 mAh g^{-1}, 450 mAh g^{-1} and 417.9 mAh g^{-1}, decaying to 388 mAh g^{-1}, 310 mAh g^{-1} and 293 mAh g^{-1} while retaining 62.5%, 68.8% and 70.1%, respectively, after 150 cycles. The sample in the case of 0.0042 mol TIPT still remained at 68% capacity at 200 cycles.

Coupled with the SEM images, we can speculate that a higher Ti content contributes to the more complete and thicker TiO$_2$ shell, which can help to continually supply a

necessary buffer space for the volume expansion of Sn when charged-discharged without collapse.
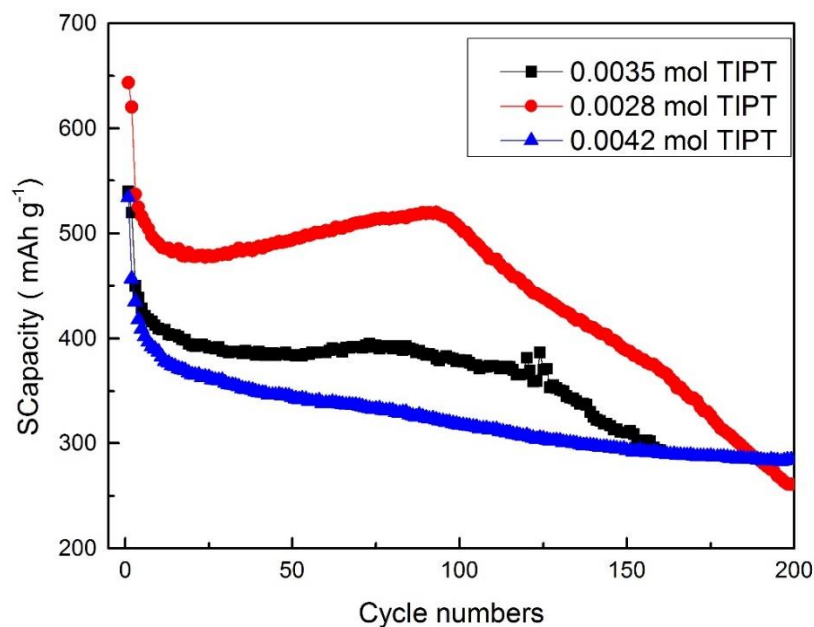
Figure 31 Specific capacity in 200 cycles of three samples obtained in the presence of 0.0028, 0.0035 and 0.0042 mol TIPT (which indicate 0.0028, 0.0035 and 0.0042 mol of Ti Content, respectively).

6. Conclusion

A new efficient and economical method to synthesize a core-shell structure composite material was introduced in this thesis. $CaCO_3$, a cheap and accessible material that is also easy to remove, is used as a template in the synthesis process. Through a series of chemical reactions and heat treatments, we obtained the target product with Sn nanoparticles attached on inner surfaces of spherical TiO_2 shells, as evidenced by SEM observation. The composition of materials was verified by XRD, XPS, and Raman. BET measurements were also used to obtain the surface area and the

pore size distribution. The TiO_2 hollow sphere structure can offer enough voids for volume expansion of tin in charge-discharge processes, which avoids the formation of cracks in tin. Therefore, the cycling performance can be improved. Compared with pure tin and other tin-based materials in the literature, the cycle performance of our samples is superior. The specific capacity of samples can be retained above 450 mAh g^{-1} at 100 cycles and 400 mAh g^{-1} at 200 cycles. These are 95% and 78.8% of the first reversible capacity, respectively.

To investigate effects of Sn and Ti content on the performance of materials, controlled experiments were designed. Through the characterization and testing, we found that a high Sn content is helpful to enhance the first cycle capacity, while a high Ti content contributes to a more stable microstructure, which improves the cycle performance of the material. However, the theoretical capacity will decrease with the increase of the Ti content. Therefore, a tradeoff between capacity and cycle performance has to be optimized.

7. Future Research

Subject to the limited time, some work was not perfect in the experiments, and there are also many questions worth studying further. A list of additional ideas is presented below.

1. As mentioned before, TiO_2 peaks in XRD spectra are shifted for some unknown

    reasons. I propose that some Sn-TiO_2 composite is formed in the synthesis process,

which requires Additional characterizationto verify the primary cause of this phenomenon.

2. To find out the reason for the capacity decay, especially after 100 cycles, I propose observing the change of microstructure and composite of the samples that charged-discharged for 2, 50, 100 and 200 cycles. Through additional characterization on the electrochemical performance, one may find out the main factors impacting the cycle performance and improve the synthesis method.

3. Various calcination and reduction temperatures and different ramp up rates can be studied. By comparing the performance and microstructure of the as-prepared samples, the optimum temperature for heat-treatment could be found.

4. Carbon/graphene coating, and nanotubes could be used to further increase the conductivity and the rate performance of these materials.

References

1. G. G. Amatucci, CoO_2, the End Member of the Li_xCoO_2 Solid Solution. *Journal of the Electrochemical Society*, 143(3): 1114–1110.

2. H. C. Choi, Y. M. Jung, I. Noda, S. B. Kim, A Study of the Mechanism of the Electrochemical Reaction of Lithium with CoO by Two-Dimensional Soft X-ray Absorption Spectroscopy (2D XAS), 2D Raman, and 2D Heterospectral XAS−Raman Correlation Analysis. *The Journal of Physical Chemistry B* 2003; 107(24): 5806.

3. R. Marom, S.F. Amalraj, N. Leifer, D. Jacob, D. Aurbach, A review of advanced and practical lithium battery materials. *J. Mater. Chem.* 2011; 21, 9938–9954.

4. G.P. Gholam Abbas Nazri, *Lithium Batteries: Science and Technology*, Kluwer Academic New York, 2003.

5. G. Girishkumar, B. McCloskey, A. C. Luntz, S. Swanson, W. Wilcke, Lithium-Air battery: Promise and challenge, *Journal of Physical Chemistry Letters*, 2010; 1(14): 2193–2203.

6. B. Scrosati, J. Garche, Lithium batteries: Status, prospects and future, *Journal of Power Sources,* 2010; 195(9): 2419–2430.

7. E. Miele, F. De Angelis, E. Di Fabrizio, R.P. Zaccaria, C. Capiglia, S. Goriparti, Review on recent progress of nanostructured anode materials for Li-ion batteries, *Journal of Power Sources*, 2014; 257.

8. H. Wu, Y. Cui, Designing nanostructured Si anodes for high energy lithium-ion

batteries, *Nano Today*, 2012; 7(5): 414–429.

9. J.R. Szczech, S. Jin, Nanostructured silicon for high capacity lithium battery anodes, *Energy & Environmental Science*, 2011; 4: 56–72.

10. R. Teki, M.K. Datta, R. Krishnan, T.C. Parker, T.-M. Lu, P.N. Kumta, N. Koratkar, Nanostructured silicon anodes for lithium-ion rechargeable batteries, *Small,* 2009; 5(20): 2236–2242.

11. A. Magasinski, P. Dixon, B. Hertzberg, A. Kvit, J. Ayala, G. Yushin, High-performance lithium-ion anodes using a hierarchical bottom-up approach, *Nature Materials*, 2010; 9(461): 353–358.

12. R. Chandrasekaran, A. Magasinki, G. Yushin, T.F. Fuller, Analysis of lithium insertion/deinsertion in a silicon electrode particle at room temperature, *Journal of the Electrochemical Society,* 2010; 157(10): A1139–A1151.

13. W. Hwang, J.K. Lee, W.Y. Yoon, Electrochemical behavior of carbon-coated silicon monoxide electrode with chromium coating in rechargeable lithium cell, *Journal of Power Sources,* 2013; 244: 620–624.

14. K. Song, S. Yoo, K. Kang, H. Heo, Y. M. Kang, M. H. Jo, Hierarchical SiO_x nanoconifers for Li-ion battery anodes with structural stability and kinetic enhancement, *Journal of Power Sources,* 2013; 229: 229–233.

15. B. Liu, A. Abouimrane, Y. Ren, M. Balasubramanian, D. Wang, Z.Z. Fang, K. Amine, New anode material based on $SiO-Sn_{30}Co_{30}C_{40}$ for lithium batteries, *Chemistry of Materials,* 2012; 24(24): 4653–4661.

16. Y. Yamada, Y. Iriyama, T. Abe, Z. Ogumi, Kinetics of electrochemical insertion

and extraction of lithium ion at SiO, *Journal of Electrochemical Society,* 2010; 157(1): A26–A30.

17. J. Yang, Y. Takeda, N. Imanishi, C. Capiglia, J.Y. Xie, O. Yamamoto, SiO$_x$-based anodes for secondary lithium batteries, *Solid State Ionics,* 2002; 152–153: 125–129.

18. I. A. Courtney, J. R. Dahn, Electrochemical and in situ x- ray diffraction Studies of the reaction of lithium with tin oxide composites, *Journal of the Electrochemical Society*, 1997; 144(6): 2045-2052.

19. H. Li, Z. Wang, L. Chen, X. Huang, Research on Advanced Materials for Li-ion Batteries, *Advanced Materials,* 2009; 21(45): 4593–4607.

20. J. Jiang, Y. Li, J. Liu, X. Huang, C. Yuan, X.W. Lou, Recent advances in metal oxide-based electrode architecture design for electrochemical energy storage, *Advanced Materials,* 2012; 24(38): 5166–5180.

21. Z. Wang, L. Zhou, X.W. Lou, Metal Oxide Hollow Nanostructures for Lithium-ion Batteries, *Advanced Materials,* 2012; 24(14): 1903–1911.

22. X. Li, C. Wang, Engineering nanostructured anodes *via* electrostatic spray deposition for high performance lithium ion battery application, *Journal of Materials Chemistry A,* 2013; 1: 165–182.

23. J. Jiang, Y. Li, J. Liu, X. Huang, C. Yuan, X.W. Lou, Recent advances in metal oxide-based electrode architecture design for electrochemical energy storage, *Advanced Materials,* 2012; 24(38): 5166–5180.

24. H. Kim, J. Cho, Hard templating synthesis of mesoporous and nanowire SnO$_2$ lithium battery anode materials, *Journal of Materials Chemistry,*

2008; 18: 771–775.

25. Z. Yang, G. Du, Z. Guo, X. Yu, S. Li, Z. Chen, P. Zhang, H. Liu, Plum-branch-like carbon nanofibers decorated with SnO_2 nanocrystals, *Nanoscale,* 2010; 2:1011–1017.

26. X. Yin, L. Chen, C. Li, Q. Hao, S. Liu, Q. Li, E. Zhang, T. Wang, Synthesis of mesoporous SnO_2 spheres via self-assembly and superior lithium storage properties *Electrochimica Acta*, 2011; 56(5):2358–2363.

27. W. M. Zhang, J. S. Hu, Tin-Nanoparticles Encapsulated in Elastic Hollow Carbon Spheres for High-Performance Anode Material in Lithium-Ion Batteries, *Advanced Materials,* 2008; 447:1160–1165.

28. J. Y. Liao, A. Manthiram, Mesoporous TiO_2-Sn/C Core-Shell Nanowire Arrays as High-Performance 3D Anodes for Li-Ion Batteries**.** *Advanced Energy Materials,* 2014; 4(14).

29. F. Gillot, J. Oro-Sole, M.R. Palacin, Nickel nitride as negative electrode material for lithium ion batteries, *Journal of Materials Chemistry,* 2011; 21:9997–10002.

30. A. Mahmoud, J.M. Amarilla, K. Lasri, I. Saadoune, Influence of the synthesis method on the electrochemical properties of the $Li_4Ti_5O_{12}$ spinel in Li-half and Li-ion full-cells. A systematic comparison, *Electrochimical Acta,* 2013; 93:163–172.

31. J. Wang, X. M. Liu, H. Yang, Characterization and electrochemical properties of carbon-coated $Li_4Ti_5O_{12}$ prepared by a citric acid sol–gel method, *Journal of Alloys and Compounds,* 2011; 509(3):712–718.

32. J.-Y. Lin, C.-C. Hsu, H.-P. Ho, S.-h. Wu, Sol–gel synthesis of aluminum doped

lithium titanate anode material for lithium ion batteries, *Electrochimical Acta*, 2013; 87:126–132.

33. P. Thomsen, C. Larsson, L. Ericson, Structure of the interface between rabbit cortical bone and implants of gold, zirconium and titanium, *Journal of Materials Science: Materials in Medicine,* 1997; 8: 653.

34. M. Winter, J. O. Besenhard, Electrochemical lithiation of tin and tin-based intermetallics and composites, *Electrochimical Acta*, 1999; 45:31-50.

35. J.W. Huang, J.Q. Zhang, SnO_x/TiO_2 composites as anode materials for lithium ion battery [dissertation]. National University of Tainan; 2014.

36. X. K. Huang, J. B. Chang, M. S. Cui, A Hierarchical Tin/Carbon Composite as an Anode for Lithium-Ion Batteries with a Long Cycle Life, *Angewandte Chemie International Edition*, 2015; 54(5): 1490-1493.

37. K. Rajkumar, P. Vairaselvi, Visible-light-driven SnO_2/TiO_2 nanotube nanocomposite for textile effluent degradation, *Royal Society of Chemistry Advances*, 2015;5: 20424-20431